Astronomy & Astrophysics manuscript no. output
April 30, 2026

Connecting the dusty dots: Dust depletion and extinction of local interstellar clouds

T. Ramburuth-Hurt[1,2], A. De Cia[3], J.-K. Krogager[4,5], C. Ledoux[6], and A. J. Fox[7]

[1] Department of Astronomy, University of Geneva, Chemin Pegasi 51, Versoix, Switzerland
[2] Wits Centre for Astrophysics, School of Physics, University of the Witwatersrand, 1 Jan Smuts Avenue, Johannesburg, 2000, South Africa
[3] European Southern Observatory, Karl-Schwarzschild-Str. 2, 85748 Garching, Germany
[4] Université Claude Bernard Lyon 1, Centre de Recherche Astrophysique de Lyon UMR5574, 9 Av. Charles André, 69230 Saint-Genis-Laval, France
[5] French-Chilean Laboratory for Astronomy (FCLA), CNRS-IRL3386, U. de Chile, Camino el Observatorio 1515, Casilla 36-D, Santiago, Chile
[6] European Southern Observatory, Alonso de Córdova 3107, Vitacura, Casilla 19001, Santiago, Chile
[7] AURA for ESA, Space Telescope Science Institute, 3700 San Martin Drive, Baltimore, MD 21218, USA

Received xx; accepted yy

ABSTRACT

Investigating the chemical complexity of the interstellar medium (ISM) is key for understanding its physical nature and evolution. In this work, we studied parsec-scale interstellar dust clouds in the neutral ISM of the Milky Way using two different probes: dust depletion and dust extinction. We examined their relationship to investigate the distribution of metals and dust in the solar neighbourhood and how they are related to the Local Bubble. We used dust depletion measurements for individual gas clouds along eight lines of sight towards bright O/B stars within 1.1 kpc of the Sun, derived from UV absorption-line spectra. We combined these with parsec-scale 3D dust extinction density maps out to 1.25 kpc. Based on the well-known relationship between gas and dust in the ISM, we assumed a correlation between dust depletion and dust extinction density. This assumption allowed us to infer that the absorption components are spatially associated with the peaks in dust extinction density and to pinpoint the likely locations of the gas clouds in physical space. Using the Python `scipy` package `find_peaks`, we identified peaks in the dust extinction curves, and then associated the stronger peaks with the strongest dust depletion components. Independent distance measurements along the line of sight towards one of our targets, θ^1 Ori C, validates our result and supports the reliability of our method. In our sample, the minimum distance between clouds with significantly different chemical properties (in terms of dust depletion) is $\sim$ 100pc. This gives an indication on the physical scale on which chemical mixing remains incomplete in the ISM of the Milky Way. For five of the eight targets, we report dust depletion values for gas clouds associated with the Local Bubble. Additionally, we find a velocity gradient that is consistent with the expansion of the Local Bubble, further supporting our methodology. Overall, we show that it is possible to use complementary information from dust depletion and dust extinction to build more detailed maps of ISM metal and dust distributions.

Key words. Milky Way – interstellar medium – absorption-line spectroscopy – dust extinction – dust depletion – 3D dust maps

1. Introduction

Studies of the chemical composition of the Milky Way's interstellar medium (ISM) gives us important insight into its evolution and the role of different gaseous phases in this environment. Both dust depletion and dust extinction are probes of the dust content in the ISM of galaxies. Dust extinction is a measure of how much light is absorbed by the dust in all gas phases of the ISM along the line of sight, including the cold and dense gas. In the Milky Way, dust extinction can be determined for different positions in the sky, and, with the inclusion of photometry and astrometry with Gaia, the construction of 3D dust maps is possible (Lallement et al. 2018; Green et al. 2019; Rezaei Kh. et al. 2024; Dharmawardena et al. 2024; Edenhofer et al. 2024).

Absorption-line spectroscopy is a powerful method for studying the metal content of the gas in galaxies because it gives access to the column densities of many metals (ions), and the methods of measuring the column densities are highly robust. Additionally, UV absorption-line spectroscopy is particularly valuable because the resonant lines of the most dominant ionisation states of the most abundant cosmic metals (C, O, Mg, Si, S, Fe, etc.) are available in the UV.

Dust depletion is the phenomenon whereby metals are incorporated into dust grains and are no longer observable in the gas phase (Field 1974; Savage & Sembach 1996; Jenkins 2009). The depletions of different metals correlate with each other to varying degrees depending on how easily they form dust. The measure of the relative abundances between metals with different refractory properties is therefore a measurement of the amount of dust depletion. In a method for characterising dust depletion, called the 'relative method' (De Cia et al. 2016, 2021; Konstantopoulou et al. 2022), the determination of the refractory indices of metals is based on relative metal abundances. While the initial implementation of the relative method have used [Zn/Fe] as the main tracer of the overall strength of dust depletion, the most recent implementations use all relative abundances that trace dust depletion (Konstantopoulou et al. 2024). An advantage of this method is that it does not make any assumptions on gas metallicity. An additional advantage is that with high-resolution absorption-line spectroscopy, we can dissect lines of sight, iden-

Article published by EDP Sciences, to be cited as https://doi.org/10.1051/0004-6361/202557895

tify, and study the chemical properties of individual gas components (Welty et al. 2020; Ramburuth-Hurt et al. 2023, 2025). Differences in dust depletion in individual gas components along lines of sight are washed away by the more typical studies of dust depletion, which examine the integrated line of sight (e.g. Jenkins 2009; De Cia et al. 2021; Roman-Duval et al. 2021; Ritchey et al. 2023).

The relationship between the dust probed by dust depletion and dust extinction is not well understood. Several studies that compare dust extinction based on dust depletion measured from full lines of sight ($A_{V,\,depl}$) and extinction ($A_{V,\,ext}$) in extragalactic damped Ly-α absorbers (DLAs; e.g. Savaglio & Fall 2004; Wiseman et al. 2017; Bolmer et al. 2019) often find significant scatter. Recently, Konstantopoulou et al. (2024) developed a more robust methodology for calculating $A_{V,\,depl}$ which uses all metals and the relative method for the integration of the dust-to-metal (DTM) ratio. They find that, for integrated line-of-sight measurements, $A_{V,\,depl}$ and $A_{V,\,ext}$ generally follow each other (see Fig. 7 of that paper), with the exception of systems that have the 2175Å bump in their extinction curve, possibly associated with polycyclic aromatic hydrocarbon (PAHs) dust particles. In these cases, Konstantopoulou et al. (2024) find that $A_{V,\,ext} > A_{V,\,depl}$. This inequality could be caused by a large amount of PAHs in the cold neutral medium (CNM), which is captured by dust extinction measurements but not by dust depletion. Dust depletion traces the dust that can be probed by metal absorption lines present in the warm neutral medium (WNM). In the Milky Way, the 2175 Å bump is generally ubiquitous (Savage & Mathis 1979; Pei 1992; Gordon et al. 2003).

Three-dimensional dust maps of the Milky Way make it possible to locate regions of the ISM with high dust content along lines of sight (Lallement et al. 2018; Green et al. 2019; Leike et al. 2020; Rezaei Kh. et al. 2024; Dharmawardena et al. 2024; Edenhofer et al. 2024). These maps have enabled detailed studies of phenomena such as the Local Bubble, including its geometry and origin. The Local Bubble is a supernova-driven, low-density cavity with a diameter of a few hundred parsecs, within which the Sun resides (Fuchs et al. 2006; Zucker et al. 2022; O'Neill et al. 2024). Zucker et al. (2022) show that several nearby star-forming regions are located on the surface of the Local Bubble. A recent study by O'Neill et al. (2024), based on the 3D dust map of Edenhofer et al. (2024), shows a chimney-like structure, likely produced by the bursting of the supernova-driven bubble.

Direct comparisons between dust extinction and dust depletion in individual ISM components along lines of sight have, to our knowledge, not been done before. This is likely because both the method of calculating the dust depletion for individual components (De Cia et al. 2016; Ramburuth-Hurt et al. 2023, 2025) and the availability of high spatial resolution 3D dust extinction maps (e.g. Lallement et al. 2018; Green et al. 2019; Leike et al. 2020; Rezaei Kh. et al. 2024; Dharmawardena et al. 2024; Edenhofer et al. 2024) are relatively recent.

In this paper, we compare these two tracers of dust – dust depletion and dust extinction – between ISM components to investigate their relationship and the possibility of cross-matching strong features in the dust extinction density with components identified from metal absorption lines. We adopt the dust depletion measurements of individual gas components along eight lines of sight from Ramburuth-Hurt et al. (2025, henceforth R-H+25) and the 3D dust extinction density maps from Edenhofer et al. (2024, henceforth E+24).

2. Data

2.1. Dust depletion

The dust depletion measurements for individual (groups of) components $[\mathrm{Zn/Fe}]_{i,\mathrm{fit}}$ were taken from the eight lines of sight in R-H+25 (see Table 1). Here, gas components refer to contributions from gas clouds along the line of sight to the overall metal absorption profile, each of which can be fitted with a Voigt profile in velocity space. Because the decomposition of lines is not unique, R-H+25 merged individual components into groups with similar velocities such that their total column densities could be robustly determined. The choice of grouping can be somewhat arbitrary and is a conservative representation of the distribution of individual components along the line of sight. We describe this in more detail in Sect. 3.

2.2. Dust extinction density

We obtained dust extinction density distributions from E+24, who mapped the dust extinction density within 1.25 kpc of the Sun. These maps have an angular resolution of 14 arcsec and parsec-scale distance resolution. From the library of available 3D dust maps, we chose E+24 due to its small angular resolution, making it most comparable to the pencil-beam measurements from absorption-line spectroscopy. E+24 is also based on the Zhang et al. (2023) catalogue from the most recent Gaia data release (DR3; Gaia Collaboration et al. 2023) out to 1.25 kpc, which contains all R-H+25 targets. This catalogue provides distance and extinction measurements for 220 million stars, with the added advantage of small extinction uncertainties (< 0.06 mag) for 87 million of these.

Zhang et al. (2023) report the parameter 'extinction' in terms of E, which is expressed in units of magnitudes and is roughly equal to the reddening $E(B-V)$. Because Zhang et al. (2023) assume a universal extinction curve $R(\lambda)$ [1], the value of E can be translated to an extinction value at a given wavelength λ. This means that E is essentially a scalar reddening factor applied to the stellar spectrum through the assumed $R(\lambda)$. We accessed the E+24 dust extinction density curves, i.e. E per parsec as a function of heliocentric distance, using the `dustmaps` Python module (Green 2018), in which we queried for each line of sight by their Galactic coordinates.

3. Methods

Our aim is to investigate whether we can pinpoint the locations of the absorbing gas clouds (groups thereof) identified in absorption by cross-matching them with peaks in dust extinction density maps. We adopted the column densities and dust depletion measurements for individual components $[\mathrm{Zn/Fe}]_{\mathrm{fit},i}$ from R-H+25.

We smoothed the dust extinction density maps using a Gaussian kernel of 4 pc to reduce the impact of noise in the peak detection process, and we set the detection prominence at 2.04×10^{-6} E/pc (following the parameters in O'Neill et al. 2024). We then identified the peaks using the `scipy` python package `find_peaks`. O'Neill et al. (2024) used this methodology to construct the geometry of the Local Bubble, where they define its shell as the first significant peak (with a Gaussian kernel of 7 pc and prominence of 2.04×10^{-6} E/pc) in extinction density along the lines of sight. We found the same first peaks as O'Neill

[1] Available at `https://zenodo.org/records/7811871`

Table 1: Details of the eight lines of sight studied in this paper, including the dust depletion measurements for individual (groups of) components from R-H+25.

Target	Distance (pc)[1]	Galactic *l, b* (deg)	A_V (mag)[2]	Group	Dust depletion	Velocity range (km s^{-1})
θ^1 Ori C	393^{+18}_{-20}	209.01, −19.38	1.78±0.36	1	1.30±0.15	[−2.1, 14.1]
				2	1.46±0.20	[16.6, 25.4]
				3	0.74±0.10	[28.0, 32.0]
				4	0.60±0.21	[35.5, 40.2]
HD 110432	439 ± 15	302.0, −0.20	–	1	1.80±0.59	[−10.1, −6.4]
				2	1.84±0.06	[−1.0, 8.2]
ρ Oph A†	137 ± 3	353.69, 17.69	2.58±0.34	1	1.32±0.18	[−29.2, −20.4]
				2	[2.0]	[−13.4, −0.3]
χ Oph	152 ± 5	357.93, 20.68	–	1	1.03±0.13	[−33.0, −22.4]
				2	1.79±0.04	[−20.8, −15.3]
				3	2.03±0.13	[−12.7, −6.4]
				4	1.70±0.16	[−4.5, 0.7]
HD 154368	1030^{+38}_{-33}	349.97, 3.22	2.53±0.20	1	1.58±0.08	[−27.7, −20.7]
				2	1.62±0.20	15
				3	0.80±0.20	[−11.3, −9.3]
				4	1.85±0.09	[−6.5, 0.1]
				5	1.22±0.27	[4.2, 13.1]
κ Aql	506^{+53}_{-41}	31.77, −13.29	–	1	0.96±0.11	[−28.2, −18.2]
				2	1.74±0.09	[−16.2, −11.1]
				3	1.60±0.06	[−8.7, −6.2]
				4	1.09±0.28	[−2.1, 1.5]
				5	0.63±0.06	[5.8, 13.9]
HD 206267	790^{+171}_{-113}	99.29, 3.74	1.47±0.14	1	1.41±0.07	[−32.1, −36.7]
				2	1.2±0.05	[−14.6, −5.3]
HD 207198	978^{+34}_{-27}	103.14, 6.99	1.50±0.29	1	1.25±0.25	[−34.3, −27.8]
				2	1.55±0.14	[−22.1, −9.8]
				3	0.87±0.49	4.7

† The square brackets for the second component along the line of sight towards ρ Oph A indicate that the dust depletion measurement for this component is unconstrained due to the saturation of most metal absorption lines.
[1] Distances are from the Sun and taken from Gaia DR3 (Bailer-Jones et al. 2021).
[2] Valencic et al. (2004).

et al. (2024) using a Gaussian kernel of 4 pc, with the benefit of detecting relevant additional peaks beyond the first.

Along the line of sight to θ^1 Ori C, we included an additional 'peak' at the stellar distance. Although no distinct peak appears in the dust extinction density profile, there is a sharp increase in this region, indicating the existence of a dense dust cloud. To ensure accurate capture of the dust contribution, we considered the dust extinction density at the upper limit of the stellar distance uncertainty as a lower bound.

We converted the UV components from velocity space to heliocentric distance under the assumption that their kinematics are due to a flat Galactic rotation curve $R = 234.88/\omega_R$ (Clemens 1985), with $R_\odot = 8.15$ kpc and $v_\odot = 236$ km/s (Reid et al. 2019). We find no plausible physical solutions from this exercise, likely because the clouds are very close by. As a result, their relative motions result from local effects rather than global Galactic rotation. All our targets are also on the same side of the Milky Way and thus do not rotate relative to each other.

To quantify the relationship between the dust depletion of absorbing gas components and peaks in dust extinction density, we assumed that dust and gas are broadly correlated, so that the absorption components with the highest level of dust depletion trace the strongest dust extinction peaks. This assumption is based on the well-known relationship between gas and dust in the ISM (Bohlin et al. 1978; Cardelli et al. 1989), which gives the average value of the Galactic gas-to-dust ratio, $N(\mathrm{H\,I})/E(B-V) = 5.8 \times 10^{21}$ cm^{-2} mag^{-1}. We expect the correlation between dust depletion $[\mathrm{Zn/Fe}]_{\mathrm{fit},i}$ and dust extinction density to be stronger than that between $[\mathrm{Zn/Fe}]_{\mathrm{fit},i}$ and dust extinction (A_V) itself. This is because depletion represents the average number of dust particles per unit length of absorbing cloud along the line of sight. As such, it is more closely related to dust extinction density than to dust extinction, which reflects the integrated amount of dust.

For each line of sight, we arranged both quantities in descending order and paired them accordingly, so that the strongest dust depletion component would be paired with the strongest dust extinction component, and so forth. We ensured consistent comparison by including only the top n values of each, where n is the smaller number of components or peaks along the line of sight. We excluded the line of sight towards ρ Oph A because it has only one constrained dust depletion component due to the saturation of many of its metal absorption lines. We then inferred the locations of the absorption components in physical space.

We estimated the minimum distance over which chemical mixing in the ISM is incomplete by comparing pairs of absorbing gas components along each line of sight and by determining whether their dust depletion $[\mathrm{Zn/Fe}]_{\mathrm{fit},i}$ differ significantly. We determined the statistical significance of the difference in $[\mathrm{Zn/Fe}]_{\mathrm{fit},i}$ for components A and B using a z-test: $\sigma_{\mathrm{z-test}} = \frac{[\mathrm{ZnFe}]_{i,A} - [\mathrm{ZnFe}]_{i,B}}{\sqrt{Err([\mathrm{ZnFe}]_{i,A})^2 + Err([\mathrm{ZnFe}]_{i,B})^2}}$, where $[\mathrm{ZnFe}]_{i,A}$ and Err ($[\mathrm{ZnFe}]_{i,A}$) are the dust depletion value and its uncertainty, respectively. We consider two components to have significantly different $[\mathrm{Zn/Fe}]_{\mathrm{fit},i}$ if $\sigma_{\mathrm{z-test}} > 3$.

4. Results and discussion

We find overall agreement between the number of absorption components (or groups thereof) and the number of peaks in dust extinction density, i.e. within ± 1 – 2, for six of the eight lines of sight in our sample (θ^1 Ori C, HD 110432, ρ Oph A, HD 154368, χ Oph, and κ Aql; see Table 2). For the lines of sight towards both HD 206267 and HD 207198, we find many more extinction peaks than absorption components. There are several possible explanations for this. The broader field of view in dust extinction measurements compared to the narrow pencil-beam nature of absorption-line spectroscopy can result in extinction that includes more clouds along the line of sight. It is also likely that peaks in dust extinction density may correspond to regions at the same velocity; hence, the absorption profile becomes blended. Extinction also typically captures the contribution from the dust present in the CNM, (e.g. PAHs). Our method of determining dust depletion is not sensitive to PAHs and carbonaceous dust because the carbon absorption line is generally saturated. Another possible explanation is that components with lower dust depletion levels are either lost in the noise or contribute less significantly to the overall dust compared to PAHs. We also note that our grouping of absorption components is conservative and therefore does not fully represent the substructure of the gas along lines of sight.

We find relatively small scatter in the overall relation between dust depletion and dust extinction density across all lines of sight, as shown in Fig. 1. Although we somewhat built in the correlation between dust depletion and dust extinction density along each line of sight by assigning the components with the strongest depletion to the clouds with the highest dust extinction density, the normalisation and slope of these correlations remained free to vary. In principle, they may be different from one line of sight to another. However, we find a strong Spearman rank coefficient of 0.81 ($p = 1.6 \times 10^{-5}$) across all lines of sight, which indicates that components with higher dust depletion likely correspond to higher dust extinction densities. The fact that all lines of sight individually display similar positive correlations is encouraging and likely represents a physical link between the two parameters. We also find a moderate Pearson correlation coefficient of 0.63 (p = 0.003) between dust depletion and dust extinction density, which suggests that the relationship between the two is unlikely to be linear.

To quantify the significance of the scatter between $[\mathrm{Zn/Fe}]_{\mathrm{fit},i}$ and log (E density), as shown in Figure 1, we conducted a Kolmogrov-Smirnov (KS) test on the normalised orthogonal residuals of the best-fit line for the relationship between dust extinction density and dust depletion. Our KS test yields a p-value of $p_{KS} = 0.79$, indicating that the normalised orthogonal residuals are consistent with a normal Gaussian distribution. Therefore, the scatter can be fully explained by the noise in the data. We provide a full analysis in Appendix A.

We used the correlation between dust extinction density and dust depletion to then infer that the locations of the gas cloud coincide with the dust extinction density peaks along each line of sight in descending order (see Sect. 3). These results are presented in Table 2. Some distances are larger than the corresponding stellar distances in Table 1; however, these reflect the combined uncertainties of the stellar distances and dust extinction maps.

For the line of sight towards θ^1 Ori C, we find that the region with the highest dust extinction density is located at around 411 pc, which coincides with the distance of the Orion Nebula itself. Furthermore, the absorption component with the highest level of dust depletion (here, component 2 with a velocity range of 17 – 25 km s^{-1} and $[\mathrm{Zn/Fe}]_{\mathrm{fit},2} = 1.46 \pm 0.20$), also resides within the nebula. This has been shown through independent studies of absorption lines towards both θ^1 Ori C, a star within the Orion Nebula, and the nearby star ι Ori, a star in the nebula's foreground (Price et al. 2001, Dalla Pola 2024 Master's thesis). The agreement between the distance to the highest extinction density peak and the absorption component exhibiting the highest level of dust depletion strongly supports our methodology. As demonstrated by R-H+2025, this absorption component also likely exhibits a high gas fraction and super-solar metallicity.

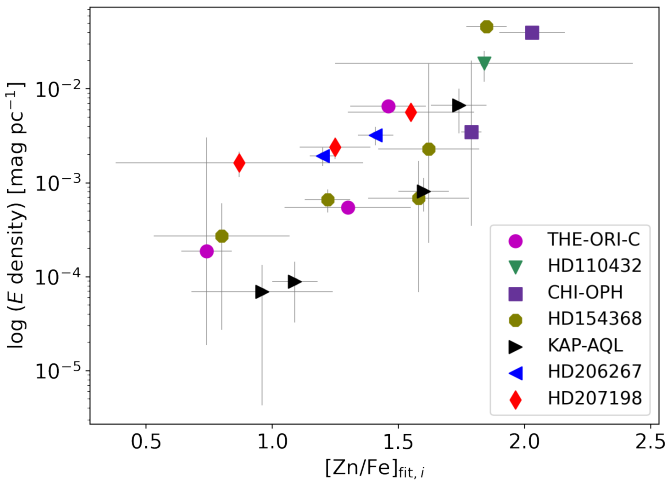

Fig. 1: Comparison of dust extinction densities with dust depletion $[\mathrm{Zn/Fe}]_{\mathrm{fit},i}$ levels for individual (groups of) gas components across all lines of sight in our sample.

Along the line of sight towards θ^1 Ori C, the distance between components 1 and 3 is the smallest observed, and their dust depletion levels differ significantly ($\sigma_{\mathrm{z-test}} = 3.1$). At distances of 159 pc and 257 pc, components 1 and 3 exhibit $[\mathrm{Zn/Fe}]_{\mathrm{fit},2} = 1.46 \pm 0.20$ and $[\mathrm{Zn/Fe}]_{\mathrm{fit},3} = 0.74 \pm 0.10$, respectively. Their difference in dust depletion, 0.56 ± 0.25, occurs over a distance of 98 pc. This distance suggests incomplete chemical mixing. While the actual scale could be even smaller, our approach effectively constrains the physical scale of gas, metal, and dust mixing. Indeed, (Redfield & Linsky 2008) find significant differences in the gas-phase abundances of Fe and Mg between the two interstellar gas clouds, the Local Interstellar Cloud and Cloud G, which are separated by only 1 pc. They attribute these differences to dust depletion, suggesting that this separation distance may also reflect incomplete chemical mixing.

In the top panels of Figs. 2 – 9 we show the absorption line profiles for Ca II λ3934 and λ3969, where available for each line of sight, as reported by R-H+25. These spectra have the highest spectral resolution and therefore most clearly demonstrate the individual components. The spectra for θ^1 Ori C, HD 110432, χ Oph, ρ Oph A, and κ Aql were taken from VLT/ESPRESSO (ID: 0102.C-0699(A), $R \sim 190000$, FWHM ~ 1.54 km s^{-1}). For HD 154368 and HD 206267, the spectra were taken from the Kitt Peak National Observatory (KPNO) Coude Feed Telescope Camera 6 ($R \sim 220\,000$, FWHM ~ 1.35 km s^{-1}). For HD 207198, we used the Ti II λ3384 line from VLT/UVES (ID 194.C-0833, $R \sim 92600$, FWHM ~ 3.2 km s^{-1}) due to the lack of available Ca II data. For some targets, we also include an additional metal absorption line to account for very weak compo-

Table 2: $[Zn/Fe]_{fit,i}$ values, corresponding dust extinction densities, and distances from the Sun for each line of sight.

Target	$[Zn/Fe]_{fit,i}$	log E density (mag pc^{-1})	Distance (pc)
θ^1 Ori C	1.46 ± 0.20	> −2.18	∼ 411.0
	1.30 ± 0.15	−3.26 ± 0.23	159.0 *(LB)*
	0.74 ± 0.10	−3.73 ± 0.18	257.0
	0.60 ± 0.21	–	–
HD 110432	1.84 ± 0.06	−1.73 ± 0.16	196.5 *(LB)*
	1.80 ± 0.59	–	–
ρ Oph A [†]	[2.0]	−2.44 ± 0.26	121.2 *(LB)*
	1.32 ± 0.18	–	–
χ Oph	2.03 ± 0.13	−1.4 ± 0.18	150.1
	1.79 ± 0.04	−2.46 ± 0.23	113.9 *(LB)*
	1.70 ± 0.16	–	–
	1.03 ± 0.13	–	–
HD 154368	1.85 ± 0.09	−1.33 ± 0.15	201.2
	1.62 ± 0.20	−2.64 ± 0.19	259.0
	1.58 ± 0.08	−3.16 ± 0.22	154.1 *(LB)*
	1.22 ± 0.27	−3.18 ± 0.22	898.9
	0.80 ± 0.20	−3.56 ± 0.29	509.4
	–	−4.0 ± 0.29	1061.6
κ Aql	1.74 ± 0.09	−2.17 ± 0.22	135.6 *(LB)*
	1.60 ± 0.06	−3.09 ± 0.17	281.2
	1.09 ± 0.28	−4.05 ± 0.28	466.0
	0.96 ± 0.11	−4.16 ± 0.41	527.6
	0.63 ± 0.06	–	–
HD 206267 [††]	1.41 ± 0.04	−2.49 ± 0.2	461.5
	1.20 ± 0.05	−2.71 ± 0.16	247.9 *(LB)*
	–	−2.96 ± 0.17	340.2
	–	−3.14 ± 0.3	515.7
	–	−3.32 ± 0.2	606.2
	–	−3.48 ± 0.18	722.0
HD 207198 [‡]	1.55 ± 0.14	−2.25 ± 0.18	425.0
	1.25 ± 0.25	−2.62 ± 0.32	616.3
	0.87 ± 0.49	−2.78 ± 0.16	227.6
	–	−3.12 ± 0.28	368.6
	–	−3.34 ± 0.29	541.8
	–	−3.73 ± 0.26	177.2 *(LB)*
	–	−3.93 ± 0.24	912.4

Notes. [(LB)] The component associated with the Local Bubble. [(†)] Results tabulated for ρ Oph A. Note that we have not associated either absorption component with dust extinction density peaks for this line of sight. [(††)] Results tabulated for HD 206267 and HD 207198. Note that the significant mismatch between the number of absorption components and dust extinction density peaks makes these results difficult to interpret.

nents in the Ca II line. These were taken from HST/STIS (ID: 16750, $R \sim 114\,000$, FWHM ∼ 2.63 km s^{-1}).

The bottom panels of Figs. 2 – 9 show the dust extinction density curves along each line of sight from E+24 in log scale. The peaks in dust extinction density are plotted as vertical dashed lines (see also Table 2). As mentioned in Sect. 3, some broader peaks may result from the combination of two or more closely spaced components. Consequently, the number of peaks counted are regarded as lower limits. To show the overall distribution of dust extinction densities, we plot the dust extinction density of each identified peak along our lines of sight in Fig. 10.

We include 2D dust maps around each of the targets in our sample in Fig. 11. These were produced by integrating the E+24 3D dust maps over the distance between the Sun and the star.

The innermost 69 pc of the dust extinction density curves was removed by E+24 due to an artificial spike in dust extinction density produced by their models in the regions closest to the Sun. This spike stems from their methodology's inclusion of the very low extinction values from Zhang et al. (2023). Since previous studies show that these nearby regions are essentially dust free (Leike et al. 2020), this exclusion affects neither their dust maps significantly overall, nor the results in our paper.

This analysis is based on a single $R(\lambda)$ law, as assumed in Zhang et al. (2023). The value $R(V)$ represents dust grain size in the ISM, with higher $R(V)$ values indicating larger dust grains. Variations around the canonical Milky Way value of $R(\lambda) = 3.1$ across different lines of sight have been shown to be small, $\sigma(R(\lambda)) = 0.18$, with less than one percent exhibiting $R(\lambda) > 4$ (Schlafly et al. 2016). Different values of $R(\lambda)$ would change E by a small factor, which would not affect the matching of absorption components with dust extinction density peaks. There could be an impact, however, on the overall relation between dust depletion and dust extinction density presented in Fig. 1, where the E values for different lines of sight could vertically shift by a small factor. This could especially be the case for the gas clouds (i.e. those clouds along the line of sight towards θ^1 Ori C) in or near the Orion Nebula, a region known for its high dust content.

ρ Oph A is the nearest target. R-H+25 were not able to perform a component-by-component analysis for this line of sight due to saturation in most of the metal absorption lines and were only able to constrain $[Zn/Fe]_{fit,i}$ for one of the components. We deduce that this results from the large amounts of gas and metal content along this line of sight. Indeed, this line of sight has high overall dust extinction $A_V = 2.58 \pm 0.34$ (Valencic et al. 2004). The dust extinction density map towards ρ Oph A also exhibits a relatively high peak at a distance of 121.2 pc from the Sun. This shows that, in addition to there being a lot of gas along this line of sight, there is also a significant amount of dust.

χ Oph is the second nearest target in our sample (after ρ Oph A), located at a distance of 152 ± 5 pc. Along this line of sight lies the component with the highest amount of dust depletion ($[Zn/Fe]_{fit,2} = 2.06 \pm 0.16$) and the highest peak in dust extinction density at a distance of 150.1 pc (see Fig. 5). This peak also exhibits one of the highest dust extinction densities, making this line of sight remarkably dust and gas rich.

The line of sight towards HD 154368 has many absorption components, which is also a feature of the dust extinction density curve (see Fig. 6). The dust cloud contributing the majority of dust extinction lies at 201.2 pc. This is one of the densest in our sample, and we associate it with the absorption component with the highest level of dust depletion along this line of sight, $[Zn/Fe]_{fit,4} = 1.85 \pm 0.09$.

The lines of sight towards both HD 206267 and HD 207190 significantly exhibit more peaks in extinction density than groups of absorption components. According to R-H+25, these two lines of sight are chemically similar. Both lie in regions of high dust extinction, as shown in the 2D dust maps of E+24 and in the relevant panels of Fig. 11. This means that the dust extinction density maps likely encompass dust clouds adjacent to these lines of sight in addition to those observed only in absorption. It is also possible that the grouping of absorption components is overly conservative and thereby miss some of the substructures along the lines of sight. HD 206267's Ca II absorption line is indeed broad and could have additional blended absorption lines (see the top panel of Fig. 8).

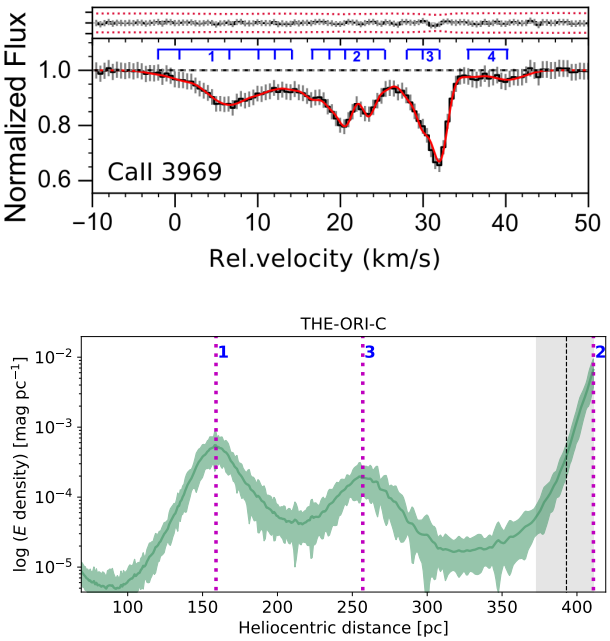

Fig. 2: Top: Ca II absorption line for θ^1 Ori C (solid black line, lower panel). The solid red lines represent the fitted Voigt profiles, obtained with `VoigtFit` (Krogager 2018) from R-H+25. The blue ticks represent the velocity-space positions of each individual component, grouped as indicated by the vertical blue lines. The values for $[Zn/Fe]_{fit,i}$ given in Table 1 correspond to the absorption groups in these figures as numbered from left to right in blue. The 1σ residuals are plotted with the black line in the upper panel of this figure, with $\pm\ 3\sigma$ marked by the dotted horizontal lines. Bottom: Dust extinction density curve in log space for the same target. The vertical dotted pink lines show the locations of the extinction density peaks. The vertical dashed black line represents the location of the star, with the uncertainties represented by the shaded region. The blue numbers correspond to the respective absorption components, as determined by our method for matching absorption components with peaks in dust extinction density (see Sect. 3).

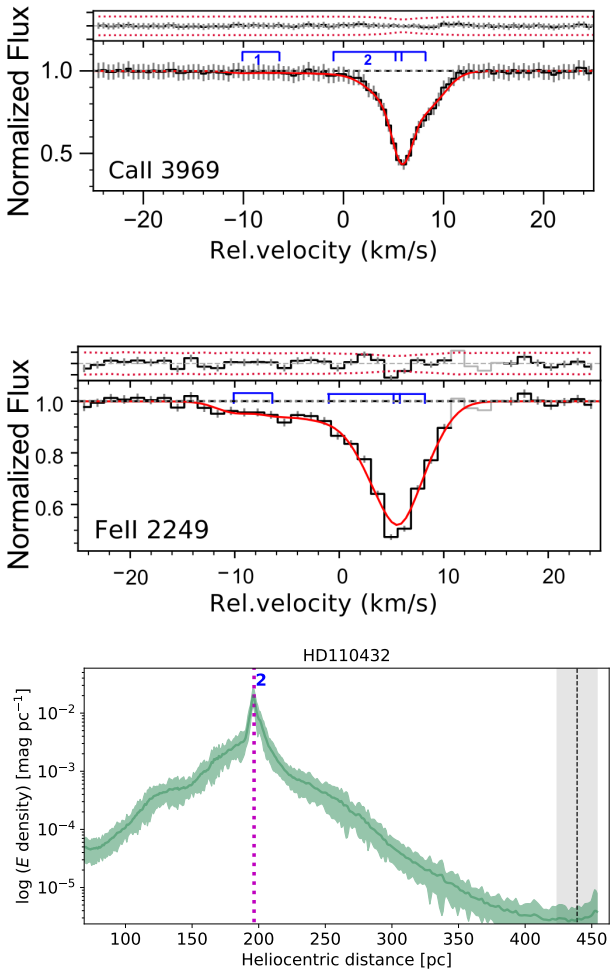

Fig. 3: Same as Fig. 5, with the addition of the Fe II λ2249 line for HD 110432.

Three-dimensional dust extinction maps have been used to study the Local Bubble in detail, enabling insights into its geometry and origin. Using the E+24 dust map, O'Neill et al. (2024) in particular show that the Local Bubble resembles a chimney, likely formed by the bursting of the supernova-driven bubble. They define the surface of the Local Bubble as the first significant peak in the E+24 dust extinction density maps along the lines of sight. Here, we use the results from our matching exercise to show the velocities of these peaks as a function of distance (solid lines in Fig. 12). We exclude the lines of sight towards HD 206267 and HD 207198 from this analysis because the mismatch between the number of absorption components and dust extinction density peaks makes them difficult to interpret.

In Fig. 12 we see that the closest components along the lines of sight towards θ^1 Ori C and HD 110432 exhibit negative velocities, while the more distant components towards ρ Oph A, χ Oph, and κ Aql show less negative or positive velocities. This pattern is consistent with a velocity gradient and can be interpreted as evidence of the Local Bubble expanding with respect to the Sun. In this frame, the Sun's motion relative to the local standard of rest (LSR; $U_\odot, V_\odot, W_\odot$ = (11.1, 12.2, 7.2) km s^{-1}; Schönrich et al. 2010) is directed towards θ^1 Ori C (−17.2 km s^{-1}) and HD 110432 (−4.5 km s^{-1}), and away from χ Oph (12.5 km s^{-1}), HD 154368 (9.2 km s^{-1}), and κ Aql (13.8 km s^{-1}). Therefore, the observed negative velocities of the nearest components are partly due to the Sun moving towards these stars. In contrast, the velocities of the more distant components appear less negative or positive, as the Sun's motion is less aligned with those directions.

These results further validate our methodology, showing that our approach to matching absorption components with dust extinction density peaks reproduces the physical structures identified in the 3D dust maps. We include Fig. 13 to show the location of the stellar targets with respect to the Local Bubble, as reported in O'Neill et al. (2024). An interactive 3D version of this plot is available online.

5. Conclusions

In this study we considered dust depletion and dust extinction as two complementary probes of interstellar dust content in individual ISM clouds (or groups thereof). We used dust depletion measurements of individual gas clouds (or groups thereof) along eight lines of sight within 1.1 kpc from the Sun (Ramburuth-Hurt et al. 2025), in combination with 3D dust extinction density maps

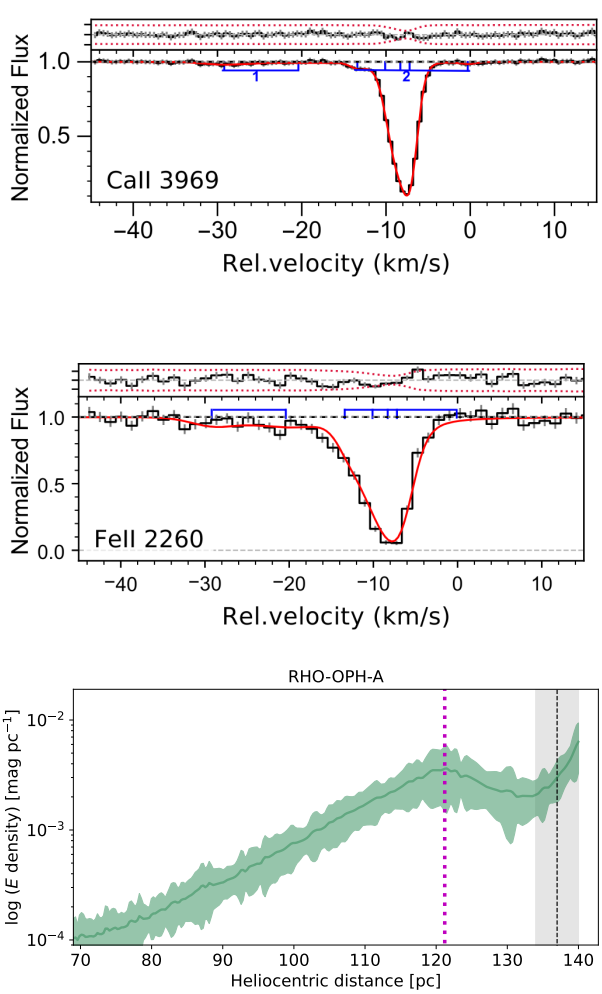

Fig. 4: Same as Fig. 5, with the addition of the Fe II λ2260 line for ρ Oph A. The dust extinction density curve is not numbered here, as we did not assign absorption components to dust extinction density peaks for this line of sight.

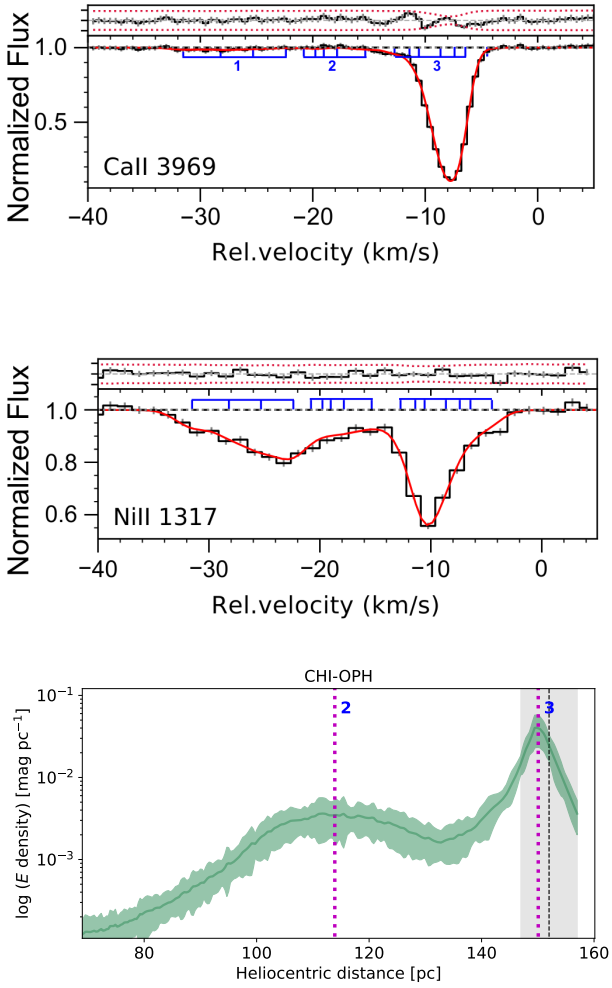

Fig. 5: Same as Fig. 2, with the addition of the Ni II λ1317 line for χ Oph.

from (Edenhofer et al. 2024). Supported by the well-known relationship between gas and dust in the ISM (Bohlin et al. 1978; Cardelli et al. 1989), we assumed a correlation between dust depletion and dust extinction density. We used this correlation to associate the absorbing clouds with peaks in dust extinction density and pinpoint the likely locations of absorption components along each line of sight. We show that different lines of sight follow a similar correlation between dust extinction density and dust depletion (see Fig. 1). This suggests that the observed relation may be physical. We find that the location of the highest dust extinction density peak coincides with an independent distance measurement of the absorption component with the highest level of dust depletion for the line of sight towards θ^1 Ori C. This agreement further corroborates our methodology.

We find that the number of absorption components (or groups thereof) and the number of peaks in the dust extinction density peaks generally agree within $\pm$ 1 – 2 for six of the eight lines of sight (θ^1 Ori C, HD 110432, ρ Oph A, χ Oph, HD 154368, and κ Aql). For five of these (excluding ρ Oph A), we obtain distance estimates for absorbing gas clouds along their lines of sight, including those associated with the Local Bubble.

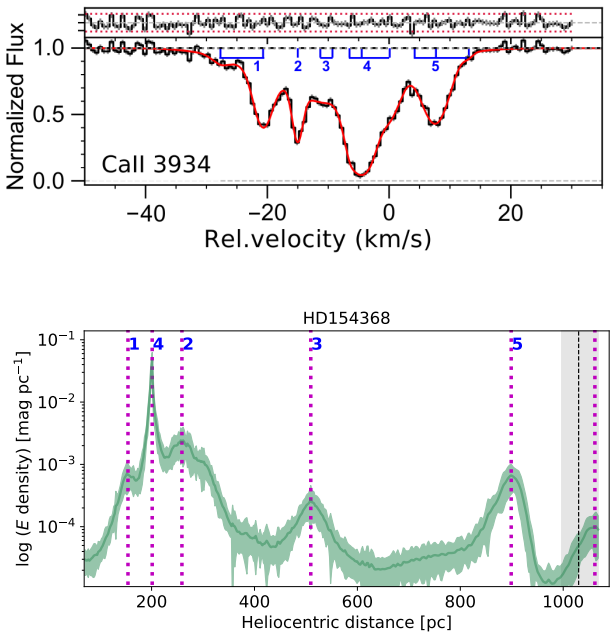

Fig. 6: Same as Fig. 2 for HD 154368.

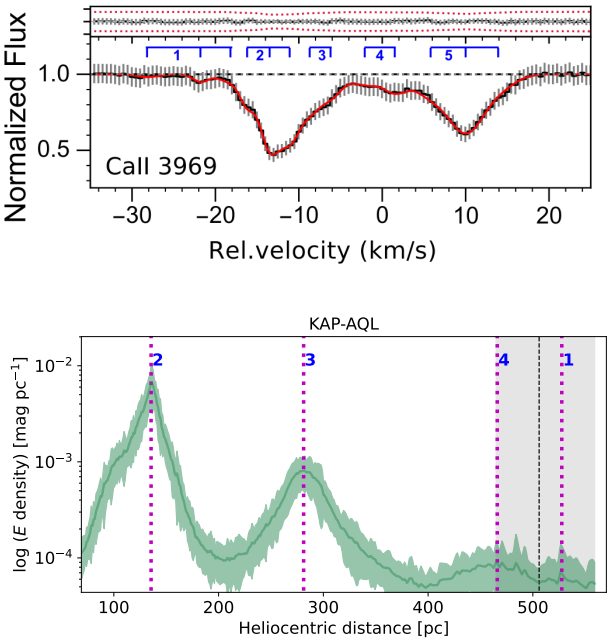

Fig. 7: Same as Fig. 2 for κ Aql.

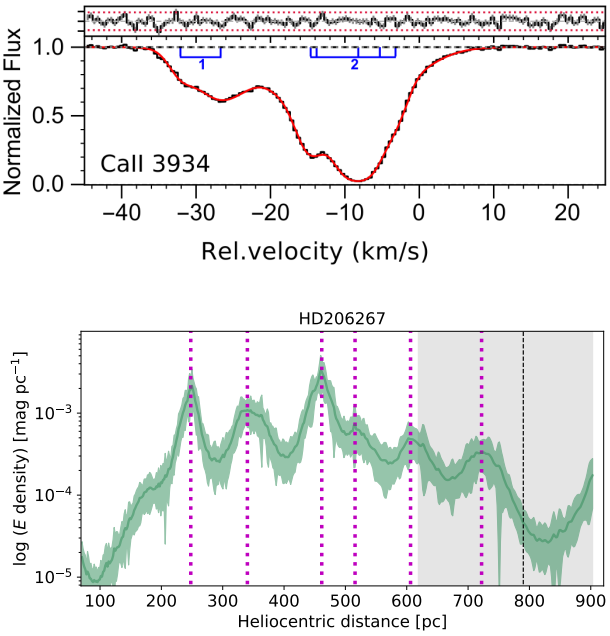

Fig. 8: Same as Fig. 2 for HD 206267. The dust extinction density curve is not numbered here due to the significant mismatch between the number of absorption components and peaks in dust extinction density, which complicates interpretation.

For the remaining two lines of sight (HD 206267 and HD 207198), we observe many more peaks in dust extinction density than groups of absorption components. This discrepancy is probably due to the blending of absorbing components that cannot be easily separated and/or the larger angular size of the dust extinction density maps, which capture more dust content than the pencil-beam of absorption-line spectroscopy.

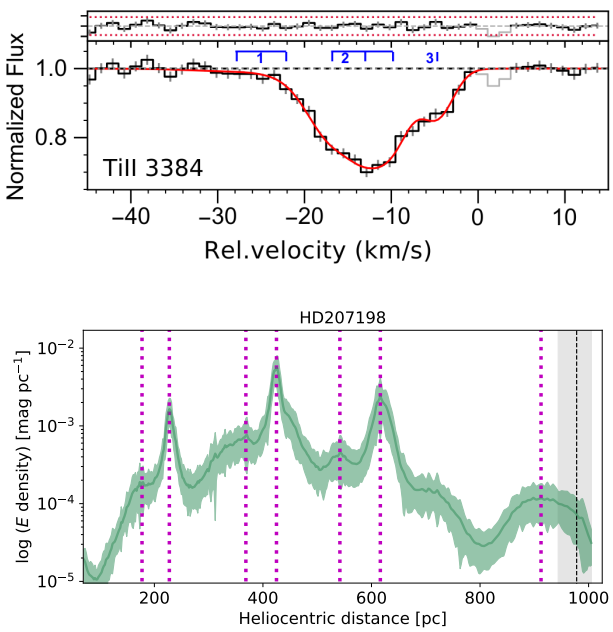

Fig. 9: Same as Fig. 2 for HD 207189. Similarly to HD 206267, the dust extinction density curve is not numbered due to the significant mismatch between the number of absorption components and peaks in dust extinction density, which complicates interpretation.

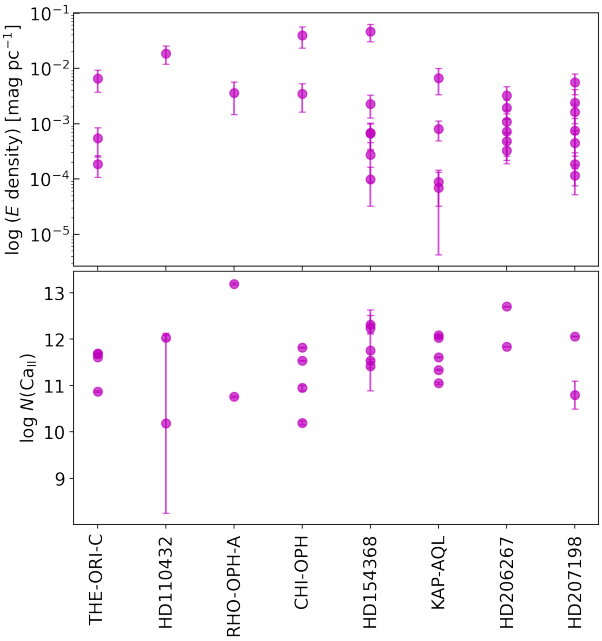

Fig. 10: Top: Distribution of dust extinction densities along each line of sight. Bottom: Distributions of Ca II column densities.

Along the line of sight to θ^1 Ori C, components 1 and 3 differ significantly in dust depletion by 0.56±0.25 over a distance of 98 pc. We interpret this as an indication of the physical scale over which chemical mixing remains incomplete in the Milky Way's ISM.

Our analysis of dust extinction and velocity structure supports the interpretation of the Local Bubble as an expanding cav-

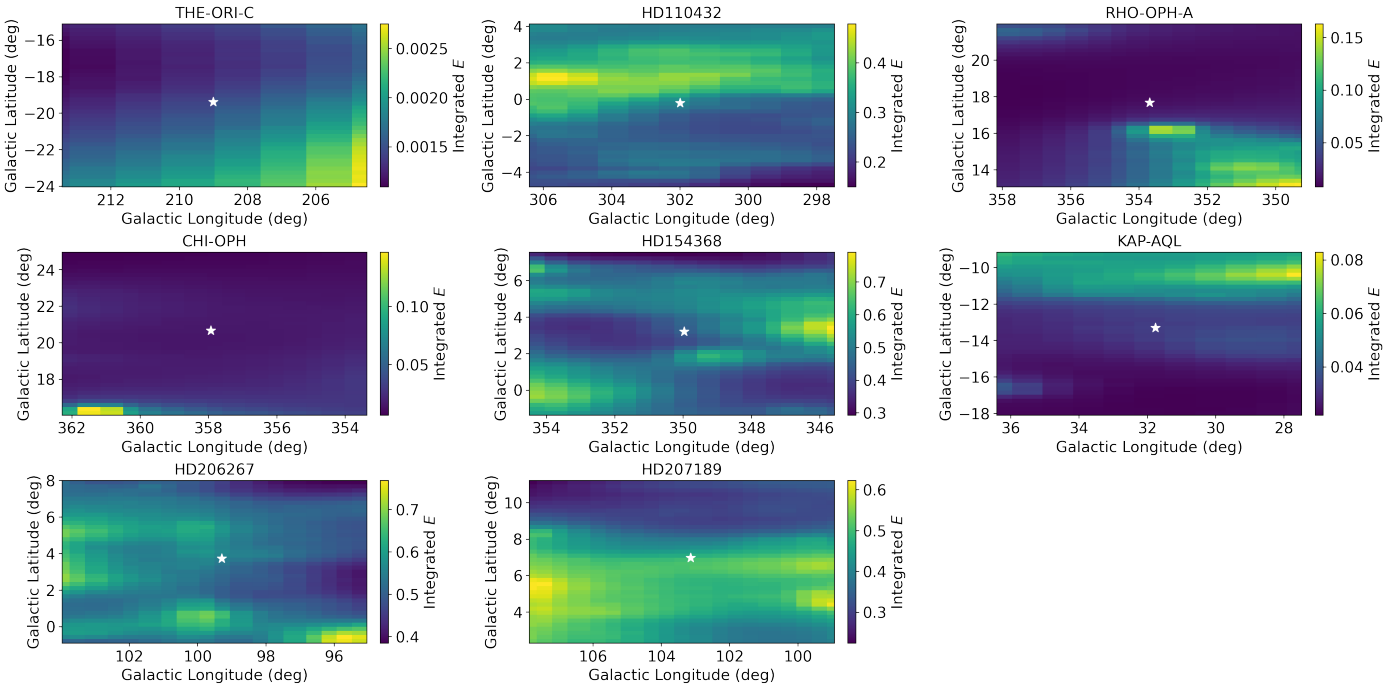

Fig. 11: 2D dust map in the region around each target taken from E+24.

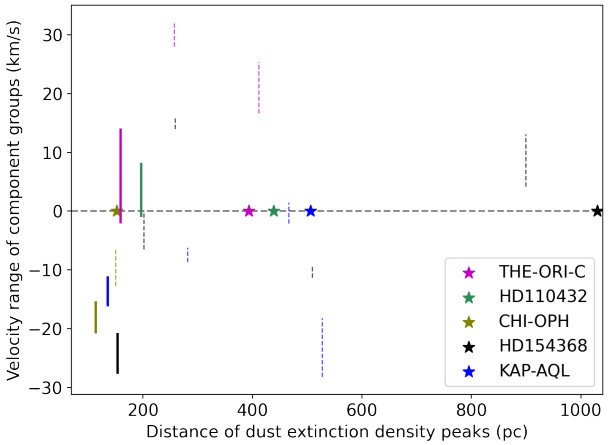

Fig. 12: Velocity as a function of distance from the Sun for gas clouds along all lines of sight. The solid lines show the clouds associated with the Local Bubble, as defined in O'Neill et al. (2024), and the dashed lines show all other clouds. The stars indicate the distances of the target stars themselves.

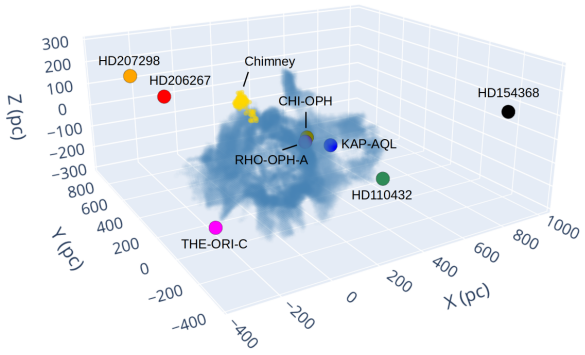

Fig. 13: 3D plot of the Local Bubble surface (O'Neill et al. 2024), shown in blue. Our stellar targets are plotted as points and labelled accordingly. The location of the chimney structure reported in O'Neill et al. (2024) is plotted in yellow and labelled accordingly. An interactive 3D version of this plot is available online.

ity surrounding the Sun. We find that Bubble's shell nearest to the Sun exhibits negative velocities, whereas the farther side exhibits less negative or positive velocities. This is consistent with an expansion-driven velocity gradient, after accounting for the Sun's motion relative to the LSR. These results further support our methodology, which matches absorption components with the highest dust depletion levels to the strongest peaks in dust extinction density along the lines of sight.

In this work, we have demonstrated the power of detailed component-by-component ISM analyses. By combining high-resolution absorption-line spectroscopy with 3D dust maps, we have provided new and invaluable insights into the nature of dust in the local ISM of the Milky Way.

Acknowledgements. T.R.-H., A.D.C., J.-K.K. acknowledge support by the Swiss National Science Foundation under grant 185692. This work is based on observations with the NASA/ESA Hubble Space Telescope obtained from Mikulski Archive for Space Telescopes at the Space Telescope Science Institute, which is operated by the Association of Universities for Research in Astronomy, Incorporated, under NASA contract NAS5-26555. This research has made use of NASA's Astrophysics Data System. The authors thank the referee, Jeffrey Linsky, for his valuable comments and feedback.

References

Bailer-Jones, C. A. L., Rybizki, J., Fouesneau, M., Demleitner, M., & Andrae, R. 2021, AJ, 161, 147
Bohlin, R. C., Savage, B. D., & Drake, J. F. 1978, ApJ, 224, 132
Bolmer, J., Ledoux, C., Wiseman, P., et al. 2019, A&A, 623, A43
Cardelli, J. A., Clayton, G. C., & Mathis, J. S. 1989, ApJ, 345, 245
Clemens, D. P. 1985, ApJ, 295, 422

De Cia, A., Jenkins, E. B., Fox, A. J., et al. 2021, Nature, 597, 206
De Cia, A., Ledoux, C., Mattsson, L., et al. 2016, A&A, 596, A97
Dharmawardena, T. E., Bailer-Jones, C. A. L., Fouesneau, M., et al. 2024, MNRAS, 532, 3480
Edenhofer, G., Zucker, C., Frank, P., et al. 2024, A&A, 685, A82
Field, G. B. 1974, ApJ, 187, 453
Fuchs, B., Breitschwerdt, D., de Avillez, M. A., Dettbarn, C., & Flynn, C. 2006, MNRAS, 373, 993
Gaia Collaboration, Vallenari, A., Brown, A. G. A., et al. 2023, A&A, 674, A1
Gordon, K. D., Clayton, G. C., Misselt, K. A., Landolt, A. U., & Wolff, M. J. 2003, ApJ, 594, 279
Green, G. M. 2018, The Journal of Open Source Software, 3, 695
Green, G. M., Schlafly, E., Zucker, C., Speagle, J. S., & Finkbeiner, D. 2019, ApJ, 887, 93
Jenkins, E. B. 2009, The Astrophysical Journal, 700, 1299
Konstantopoulou, C., De Cia, A., Krogager, J.-K., et al. 2022, A&A, 666, A12
Konstantopoulou, C., De Cia, A., Ledoux, C., et al. 2024, A&A, 681, A64
Krogager, J.-K. 2018, VoigtFit: Absorption line fitting for Voigt profiles, Astrophysics Source Code Library, record ascl:1811.016
Lallement, R., Capitanio, L., Ruiz-Dern, L., et al. 2018, A&A, 616, A132
Leike, R. H., Glatzle, M., & Enßlin, T. A. 2020, A&A, 639, A138
O'Neill, T. J., Zucker, C., Goodman, A. A., & Edenhofer, G. 2024, ApJ, 973, 136
Pei, Y. C. 1992, ApJ, 395, 130
Price, R. J., Crawford, I. A., Barlow, M. J., & Howarth, I. D. 2001, MNRAS, 328, 555
Ramburuth-Hurt, T., De Cia, A., Krogager, J. K., et al. 2025, A&A, 695, A14
Ramburuth-Hurt, T., De Cia, A., Krogager, J. K., et al. 2023, Astronomy & Astrophysics, 672, A68
Redfield, S. & Linsky, J. L. 2008, ApJ, 673, 283
Reid, M. J., Menten, K. M., Brunthaler, A., et al. 2019, ApJ, 885, 131
Rezaei Kh., S., Beuther, H., Benjamin, R. A., et al. 2024, A&A, 692, A255
Ritchey, A. M., Jenkins, E. B., Shull, J. M., et al. 2023, ApJ, 952, 57
Roman-Duval, J., Jenkins, E. B., Tchernyshyov, K., et al. 2021, ApJ, 910, 95
Savage, B. D. & Mathis, J. S. 1979, ARA&A, 17, 73
Savage, B. D. & Sembach, K. R. 1996, Annual Review of Astronomy and Astrophysics, 34, 279
Savaglio, S. & Fall, S. M. 2004, ApJ, 614, 293
Schlafly, E. F., Meisner, A. M., Stutz, A. M., et al. 2016, ApJ, 821, 78
Schönrich, R., Binney, J., & Dehnen, W. 2010, MNRAS, 403, 1829
Valencic, L. A., Clayton, G. C., & Gordon, K. D. 2004, ApJ, 616, 912
Welty, D. E., Sonnentrucker, P., Snow, T. P., & York, D. G. 2020, ApJ, 897, 36
Wiseman, P., Schady, P., Bolmer, J., et al. 2017, A&A, 599, A24
Zhang, X., Green, G. M., & Rix, H.-W. 2023, MNRAS, 524, 1855
Zucker, C., Goodman, A. A., Alves, J., et al. 2022, Nature, 601, 334

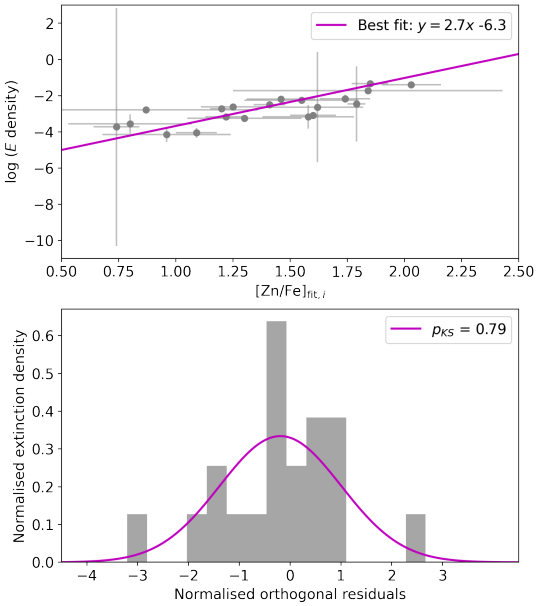

Fig. A.1: Top: Best-fit straight line to dust extinction density vs dust depletion. The plot here is the same as Fig. 1, with the inclusion of the best-fit line. Bottom: Normalised orthogonal residuals over-plotted with their Gaussian distributions.

Appendix A: Scatter analysis

Since there are uncertainties on both the dust extinction density and the dust depletion, we perform an orthogonal distance regression (ODR) fit to the data and obtain a best-fit straight line of $y = mx+b$, where $m = 2.7\pm0.4$ and $b = -6.3\pm0.6$ (see the top panel of Figure A.1). We then calculate the orthogonal residuals and normalise them by the dividing by total projected uncertainties for all data points. We find that the normalised orthogonal residuals follow a Gaussian distribution, with a KS p-value of $p_{KS} = 0.79$, as shown in the bottom panel of Figure A.1. This shows that the scatter can be fully explained by the noise in the data.